Folate-graphene chelate manganese nanoparticles as a theranostic system for colon cancer MR imaging and drug delivery: In-vivo examinations

Marzieh Samiei Foroushani[a], Reza Karimi Shervedani[a,*], Amirhosein Kefayat[b], Mostafa Torabi[a], Fatemeh Ghahremani[c], Fatemeh Yaghoobi[a]

[a] Department of Chemistry, University of Isfahan, Isfahan, 81746-73441, Iran
[b] Department of Oncology, Cancer Prevention Research Center, Isfahan University of Medical Sciences, Isfahan, 81746-73461, Iran
[c] Department of Medical Physics and Radiotherapy, Arak University of Medical Science, Arak, 38481-76941, Iran

ABSTRACT

Targeted drug delivery can improve the efficiency of therapeutic and diagnostic agents and reduce their toxicity in cancer treatments. Herein, a theranostic system based on graphene oxide (GO) integrated with polydopamine (PDA), bovine serum albumin (BSA), DTPA-Mn(II) contrast agent, folic acid (FOA) targeting agent, and 5-fluorouracil (5Fu) anticancer drug is constructed to target CT-26 colon cancer cells via folate receptors (FRs) overexpressed on cancer cells. Physicochemical characteristics of the RGO-PDA-BSA/FOA-DTPA-Mn(II)/5Fu system are studied by electrochemical and UV–Vis methods.

The system was studied based on (i) *in-vitro* and *in-vivo* MRI measurements to verify its efficiency as a *diagnostic* agent, (ii) histopathological experiments to evaluate *biocompatibility* of the system, (iii) ICP-OES analysis in conjunction with histopathological tests to find its *biodistribution*, and (iv) *in-vivo* experiments using CT-26 colon cells (tumoral animals) to show its ability for cancer *therapy*. The results show that the RGO-PDA-BSA/FOA-DTPA-Mn(II) is (i) highly promising as a contrast agent for MRI measurements ($r_1 \cong 14.7\,mM^{-1}\,s^{-1}$), (ii) biocompatible, (iii) *selectively* distributed into the CT-26 tumors compared with liver and spleen, and (iv) very effective for therapy of the colon tumors.

1. Introduction

Targeted drug delivery has received great attention as one of the most successful cancer treatment strategy in recent years [1]. In comparison with classical administration of anticancer drugs that cause nonselective action of the drug against healthy organs and cells and leading to severe side effects, the current strategy is highly promising to improve the safety, selectivity, and efficiency of the cancer treatment agents. Recently, nanotechnology has been greatly used as a fundamental tool in cancer targeting treatment [2,3]. For example, the nanomaterials functionalized with targeting moieties such as antibodies, aptamers, and small molecules have been constructed for the selective targeting and delivery of drugs into the tumor cells [4–8]. In particular, folic acid (FOA), as one of the most well-known targeting agent for cancer cells with high affinity toward folate receptors (FRs) overexpressed at the cancer cells [9–12], has been used to functionalize nanomaterials for this purpose. Moreover, nanomaterials could be used as a multifunctional base for simultaneous imaging and controlled release of drugs in the cancer sites [13,14].

Integration of both diagnostic and therapeutic components onto a single nanoplatform, known as theranostic system, has received great attentions for tumor treatment [11,12,15,16]. However, there is still a challenge to find new theranostic systems having improved diagnostic and therapeutic efficiency such as low cytotoxicity, loading of diagnostic and drug agents simultaneously, active targeting delivery, and controlled release profile [12].

With the development of graphene as a relatively new nanomaterial in recent years, researchers have explored applications of functionalized graphene derivatives in the theranostic systems [16–19]. The application of graphene as a platform for drug delivery, in conjunction with paramagnetic imaging agents, enables one to control the delivery and release process of the drugs. The large surface area and ease of surface modification of graphene allow one to load *simultaneously* high amount of *drug*, *diagnostic agents* such as magnetic resonance imaging (MRI) contrast agents, and *targeting groups* onto the platform surface. Another interesting aspect of graphene for drug delivery and cancer therapy applications is the particular arrangement of its carbon atoms, enabling the *noncovalent* immobilization of drugs onto the graphene

surface, and thus, a better control over release of drugs to the targeted tumors [19].

Recently, a new nanocomposite system based on graphene/manganese chelate was constructed, RGO-PDA-BSA-DTPA-Mn(II), and its physicochemical characteristics were fundamentally studied by our group [16]. The results showed that the fabricated nanocomposite was highly promising for immobilization of cancer theranostic agents. The need of a deep knowledge about the *in-vivo biological* behavior of the constructed system besides the necessities already discussed in above, regarding *immobilization of the targeting and therapy agents on adjacent to each other* on the nanocomposite and *in-vitro behavior of the resulted system*, encouraged us to perform the current work.

Accordingly, in the present work a theranostic system is constructed as follows: Briefly, the GO is synthesized and functionalized with polydopamine (PDA) by self-polymerization of DA onto the GO surface, leading to reduced GO modified with PDA (RGO-PDA) [20]. The PDA film stabilizes and protects the RGO, where the PDA surface groups help further to link the arriving functional groups of other constituents of theranostic system onto the RGO-PDA surface. Bovine serum albumin (BSA) biopolymer and FOA targeting agents are grafted onto the RGO-PDA surface via Michael addition and/or Schiff base reactions (using amines groups present on BSA and FOA) leading to RGO-PDA-BSA/FOA system [21]. The BSA plays a targeting as well as an antifouling role for drug delivery systems [22–24]. Therefore, utilization of the RGO-PDA-*BSA/FOA* as a *double targeted* system, in which the BSA acts as a *nutrition* source for tumors and the FOA has a high *affinity* toward FRs overexpressed at cancer cells, seems to be highly reasonable for targeted therapy applications.

The paramagnetic agent, DTPA-Mn(II) [16,25], is immobilized onto the RGO-PDA-BSA/FOA, leading to RGO-PDA-BSA/FOA-DTPA-Mn(II) system, and the resulted system is tested as a *cancer theranostic system* as follows:

The *in-vitro* and *in-vivo* MRI measurements are performed to support the efficiency of the RGO-PDA-BSA/FOA-DTPA-Mn(II) system as a *contrast agent*. To evaluate the capturing ability of the system for the cancer cells; it is loaded by 5-fluorouracil (5Fu, a model of anticancer drug) first, and then, its capturing ability is traced via *in-vivo* by using CT-26 colon cancer cells [26]. The fabrication process and physicochemical investigations together with *in-vivo* studies are presented and discussed. *Interesting results are obtained regarding in-vivo activities as the main and final part of this work.*

2. Methods and materials

2.1. Materials and reagents

Graphite powder (1–2 μm, Aldrich), dopamine hydrochloride (DA), bovine serum albumin fraction V (BSA), diethylenetriaminepentaacetic acid (DTPA), 5-fluorouracil (5Fu), folic acid (FOA), 1-ethyl-3(3-dimethylamino)-propyl) carbodiimide (EDC), Manganese(II) chloride tetrahydrate ($MnCl_2 \cdot 4H_2O$), and other chemicals were of analytical grade obtained from commercial sources (Sigma-Aldrich®, Fluka® or Merck®). All solutions were prepared with distilled water. The test solutions were deaerated with argon gas for 10 min before each electrochemical experiment and blanketed with the gas during the experiments. Phosphate buffer solution (PBS) was prepared by mixing 0.05 M KH_2PO_4/0.05 M K_2HPO_4 and the required pH was adjusted by using 0.1 M H_3PO_4 or 0.1 M NaOH. The PBS, pH 7.4, was sterilized according to our previous report [11].

2.2. Apparatus and physicochemical characterization

The UV–Vis measurements were performed by using UV–Vis–NIR spectrophotometer Cary 500.

The electrochemical measurements were performed on the Potentiostat/Galvanostat Autolab30 in a conventional three-electrode glass cell, using the modified GC disk electrode as working electrode, a Pt plate with large surface area as counter electrode, and a Ag/AgCl as reference electrode. All experiments were performed at room temperature and under argon atmosphere.

2.3. Modification of graphene surface

The synthesis steps of RGO-PDA-BSA/FOA-DTPA-Mn(II)/5Fu powder are presented in Supporting Information file, Section S1, to save the space.

2.4. Electrochemical measurements

A 1.0 mg of graphene based samples, numbered as (i) to (vi), including (i) GO, (ii) RGO-PDA, (iii) RGO-PDA-BSA/FOA, (iv) RGO-PDA-BSA/FOA-DTPA, (v) RGO-PDA-BSA/FOA-DTPA-Mn(II), and (vi) RGO-PDA-BSA/FOA-DTPA-Mn(II)/5Fu (Section S1), was dispersed into a 1.0 mL distilled water in separate vessels by using an ultrasonic bath. Then, six sets of clean GC electrodes were prepared [27] and each set was modified individually by using a 10.0 μl of the sample solutions (i) to (vi), dropped onto the clean GC electrodes and allowed to be dried under clean air. All the modified electrodes were washed with distilled water and used for the electrochemical measurements.

2.5. In-vitro 5Fu release from RGO-PDA-BSA/FOA-DTPA-Mn(II)/5Fu

The release profile of 5Fu from RGO-PDA-BSA/FOA-DTPA-Mn(II)/5Fu was carried out in PBS media at pH 7.4 and 37 °C, 30 h. The samples were filtered through a dialysis bag (MWCO: 14 kDa, Sigma), and the concentration of the released 5Fu drug was measured at the different time intervals by using a standard calibration curve constructed based on UV–Vis absorbance peak of 5Fu at 265 nm (Fig. S1).

2.6. Cell culture

The CT-26 (murine colon cancer) cell line was purchased from Pasteur Institute of Iran, Tehran. The cells were cultured in RPMI 1640 medium (Sigma, USA) containing 10% fetal bovine serum (FBS) and 1% antibiotics mixture, comprising penicillin and streptomycin. The cells were incubated at recommended conditions in a humidified incubator; 37 °C and 5% CO_2 atmosphere.

2.7. MRI measurements

(i) *In-vitro*; The aqueous suspension solutions of RGO-PDA-BSA/FOA-DTPA-Mn(II) system with different Mn(II) ion concentration, varied from 0.02 to 1.0 mM, were prepared and the MRI data were acquired.

(ii) *In-vivo*; The male Wistar rats, weighted approximately 180–200 g, were injected with RGO-PDA-BSA/FOA-DTPA-Mn(II) system (1.5 mg system/kg animal; abbreviated as 1.5 mg/kg) intravenously, and then, their MRI data were acquired using a 1.5 T S Symphony Scanner at different time intervals. Specialized MRI instruments with higher magnetic fields are more feasible for this purpose; however, such an instrument was not available to us. Thus, we set the 1.5 T MRI instrument with the smallest coils built in the machine and used for the current work. The imaging parameters were as follow: echo time = 11 ms, repetition time = 1560 ms, slide thickness = 3.5 mm, and field of view = 399 mm.

To evaluate the efficacy of the RGO-PDA-BSA/FOA-DTPA-Mn(II) system for *tumor targeting*, the CT-26 *tumor-bearing* mice were injected with the system (1.5 mg/kg) through tail vein of mice, and then, their MRI measurements were carried out under the same conditions.

2.8. Animal care and husbandry

Female BALB/c mice (6–8 weeks old, weight of 22–24 g) were purchased from the Pasteur Institute of Iran. Mice were maintained at standard conditions including 24 ± 2 °C temperature, $50 \pm 10\%$ relative humidity, and 12 h light/12 h dark. All mice were fed with sterilized standard mouse chow and water ad libitum. All procedures were verified according to the guidelines of the Institutional Animal Care and Ethics Committee of Isfahan University of Medical Sciences.

2.9. Histopathology and blood biochemistry examinations

For assessment of the RGO-PDA-BSA/FOA-DTPA-Mn(II) system toxicity, the mice were injected intravenously with the suspension solution of the system (1.5 mg/kg) prepared in 0.05 M PBS, pH 7.4. The control group mice were injected with the same volume of PBS. The injected mice were sacrificed after 20 days and their vital organs including brain, liver, spleen, lung, and kidneys were harvested to evaluate their toxicity. The harvested organs were fixed with 10% formalin neutral buffer solution for at least 24 h, and then, the treated tissues were embedded in paraffin, dehydrated, blocked and cut into 5-μm-thick sections by microtome. The sections were stained by hematoxylin and eosin (H&E) and the histological photograph of each section was recorded using an Olympus BX51 microscope coupled with an Olympus DP70 digital camera (Olympus Optical, Co. LTD, Tokyo, Japan).

2.10. Biodistribution of RGO-PDA-BSA/FOA-DTPA-Mn(II) system

In order to study the biodistribution of RGO-PDA-BSA/FOA-DTPA-Mn(II) system and its tumoral uptake, the CT-26 colon tumor-bearing mice were injected intravenously with the system (1.5 mg/kg) and sacrificed after 24 h. The liver, kidney, spleen, and tumor were weighed and digested in Aqua Regia. Finally, the mean amount of Mn(II) ion per gram of each organ was measured by ICP-OES (PerkinElmer, Optima 7300DV) technique to determine semi-quantitative biodistribution of the constructed system.

2.11. Tumor implantation and treatment

The *in-vivo* antitumor activity of the system was evaluated by using the CT-26 colon cancer-bearing mice. An amount (1×10^6) of the CT-26 colon cancer cells were suspended in 50 μL PBS and injected subcutaneously at the left flank of mice. The mice were randomly divided into different groups (n = 8), when tumors became palpable. The groups consisted of the mice injected with (X mg/kg) (i) RGO-PDA-BSA/FOA-DTPA-Mn(II) system (X = 1.5 mg/kg), (ii) RGO-PDA-BSA/FOA-DTPA-Mn(II)/5Fu system (X = 1.5 mg/kg), (iii) pure 5Fu (X = 1.2 mg/kg), and (iv) pure PBS (50 μL, 0.05 M) with an injection regime of "every 3 days and for a period of 3 weeks" for the entire samples. The size of tumors was measured by a digital caliper every 3 days and the volume of the tumor was calculated through the following modified ellipsoidal equation [28]. Tumor volume = (tumor length) × (tumor width)^2/2.

2.12. Statistical analysis

Statistical analysis was performed using JMP 11.0. All data were analyzed by One Way ANOVA. Statistical significance was set at probability (P) < 0.05. All measurements have been repeated several times on group of animals, thus the results are expressed as mean ± SD.

3. Results and discussion

3.1. Physicochemical characterization

The UV–Vis spectra obtained during step-by-step modification of GO by PDA, BSA/FOA, DTPA, Mn(II) and 5Fu species are presented in Fig. S2. The GO shows two absorption peaks around 230 and 300 nm, corresponding to the π-π* and n-π* transitions of the aromatic C–C and C═O bonds, respectively (curve a), this pattern is similar to that reported in literature [29]. After immobilization of PDA onto the RGO surface, these peaks have been merged and shifted to ~310 nm (curve b) which is in good agreement with previous reports [30]. Furthermore, the electronic absorption of the RGO-PDA in the UV–Vis region is increased significantly, compared with the GO, which is attributed to the reduced GO (i.e. formation of RGO), where the π-electronic conjugated network structure of GO is partially restored [31]. Simultaneous immobilization of BSA and FOA modifying layers onto the RGO-PDA surface have caused three characteristic absorption peaks to appear around 230, 280, and 340 nm (curve c). Since immobilization of only BSA onto RGO-PDA surface does not exhibit any characteristic absorption band (Fig. S3, curve c), these peaks are attributed to the presence of FOA on the surface; these findings are similar to previous ones [32]. Grafting of DTPA onto the RGO-PDA-BSA/FOA system led to disappearance of the absorption peaks of FOA at 230 and 280 nm, and a shift in the peak position at 345 nm to lower wavelengths (320 nm) together with a decrease in its intensity and increase its width (Fig. S2, curve d). These behaviors are explained based on the FOA position, which is now deeper in the RGO-PDA-BSA/FOA-DTPA system structure. The absorption peak at ~330 nm does not change significantly after complexation of Mn(II) ion by RGO-PDA-BSA/FOA-DTPA system. Also, immobilization of the DTPA and the complexed Mn(II) ions onto the RGO-PDA-BSA surface in the absence of FOA, does not exhibit any additional characteristic absorption peak (Fig. S3, curves d and e), compared with RGO-PDA-BSA. This behavior indicates that FOA does not interact significantly with either DTPA or Mn(II). The adsorption of 5Fu on RGO-PDA-BSA/FOA-DTPA-Mn(II) system has resulted in a characteristic peak around 265 nm (Fig. S2, curve f) [33]. Furthermore, the intensity of the peak of FOA on the RGO-PDA-BSA/FOA-DTPA-Mn(II)/5Fu system appeared around ~330 nm is still observable (is not decreased by a large amount), indicating that a fraction of the immobilized FOA functions is still active and available for next intentions. *Overall*, the UV–Vis results support successful attachment of modifying layers onto the graphene surface, interaction of the constructed system with the 5Fu, and thus, formation of the RGO-PDA-BSA/FOA-DTPA-Mn(II)/5Fu system.

One point should be mentioned here: The size of nanoparticles required for drug delivery and cancer treatment is between 70 and 200 nm, depending on the destination organ [34]. The size of particles prepared in this work is between 70 and 180 nm, implying that the fabricated system is appropriate for this purpose, as reported in the previous work [16].

To ascertain formation of modifying layers on the GO surface, the constructed systems were transferred onto the GC electrode surface and characterized by electrochemical methods directly based on Mn(III)/Mn(II) redox reaction current. The differential pulse voltammetry (DPV) measurements, performed in 0.05 M PBS, pH 7.4, in the absence of any redox probe on the (a) bare GC, (b) GC-GO, (c) GC-RGO-PDA, (d) GC-RGO-PDA-BSA/FOA, (e) GC-RGO-PDA-BSA/FOA-DTPA, (f) GC-RGO-PDA-BSA/FOA-DTPA-Mn(II) and (g) GC-RGO-PDA-BSA/FOA-DTPA-Mn(II)/5Fu electrodes are presented in Fig. 1.

While the DPV of GC electrode is featureless, GC-GO electrode shows a peak around −0.07 V, which is attributed to the redox-active carbon-oxygen groups existing at the GO surface (Fig. 1, curve a) [35]. Reduction of GO to RGO by DA and formation of RGO-PDA (Section 2.3) has led to (i) a very broad faradaic peak around −0.10 V, a shoulder around +0.4 V, and (ii) an increase in the background
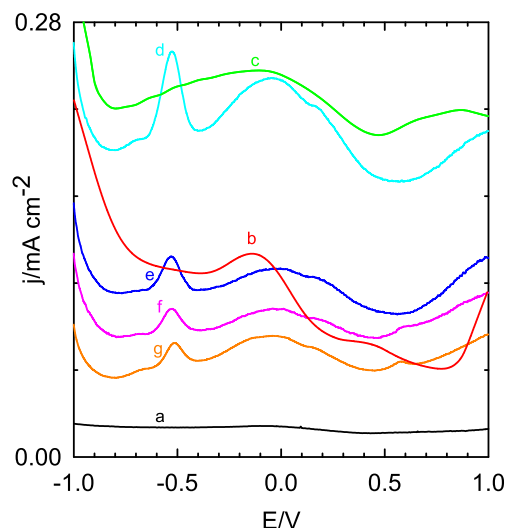
Fig. 1. The differential pulse voltammograms obtained in 0.05 M PBS, pH 7.4, in the absence of any redox probe on the (a) bare GC, (b) GC-GO, (c) GC-RGO-PDA, (d) GC-RGO-PDA-BSA/FOA, (e) GC-RGO-PDA-BSA/FOA-DTPA, (f) GC-RGO-PDA-BSA/FOA-DTPA-Mn(II) and (g) GC-RGO-PDA-BSA/FOA-DTPA-Mn(II)/5Fu electrodes.

currents for GC-RGO-PDA, compared with GC-GO electrode. These behavior can be assigned to the following aspects, respectively; (i) presence of PDA, having catechol moieties in its structure, and therefore, has resulted in significant faradaic redox reaction currents, and (ii) conversion a large amount of GO to RGO on the surface (RGO shows a larger background than GO). Still, contribution of pseudo-capacitance currents (adsorption effects coming from PDA) to the background should not be neglected (curve b) [31,36]. In the presence of BSA and FOA, simultaneously immobilized on the RGO-PDA surface, the background currents of the electrode (GC-RGO-PDA-BSA/FOA) are decreased and a faradaic peak (curve c) with a formal potential of −0.530 V, related to the direct electron transfer between immobilized FOA and the GC electrode base, is appeared [37]. Upon grafting of DTPA onto the RGO-PDA-BSA/FOA surface, the faradaic peak current of FOA is decreased, which in turn, can be due to a decrease in the number of available FOA functions on the surface. The repeatable wave observed at the formal potential of +0.520 V (curve f), is related to Mn (III)/Mn(II) redox reaction [38], and thus, supports the presence of Mn (II) ions immobilized on the RGO-PDA-BSA/FOA-DTPA-Mn(II) system. In the meanwhile, the faradaic peak current of FOA was decreased slightly because of tailoring the surface functions by the Mn(II) ions, hindering redox reaction of the immobilized FOA [11]. Finally, by adsorption of the 5Fu (the 5Fu is electrochemically inactive at these

conditions) [39] on the RGO-PDA-BSA/FOA-DTPA-Mn(II) system, the faradaic peak currents of Mn(II) and FOA are not changed significantly (curve g). This is an interesting behavior, indicating that a significant amount of FOA functions are still available and active for next intentions. These observations support those obtained by UV–Vis method (see the end of first paragraph in this Section, and Fig. S2, curve f). Thus, the electrochemical results support further the formation of system designed for theranostic intentions; RGO-PDA-BSA/FOA-DTPA-Mn(II)/5Fu.

3.2. Assessment of the biocompatibility of RGO-PDA-BSA/FOA-DTPA-Mn (II)

Toxicity is always a great concern for nanomaterial-based drug carriers used in chemotherapy; where the side effects usually limit their utilization, especially for *in-vivo* applications. Therefore, as the first step of animal experiments, biocompatibility of RGO-PDA-BSA/FOA-DTPA-Mn(II) system was deeply evaluated by histological microscopy (Section 2.9). The mice vital organs were examined 20 days after injection of the system. The system did not exhibit any toxicity or organ damage according to H&E sections during this time (Fig. 2). No obvious sign of toxicity was also observed for mice injected by nanodrugs based on graphene using the histology examination [40], *demonstrating high biocompatibility for the system, which makes it a promising candidate for drug delivery applications*.

3.3. Biodistribution of RGO-PDA-BSA/FOA-DTPA-Mn(II) system

3.3.1. Biodistribution assessment based on histopathological examinations; the role of FOA

One of the most determinative properties for drug delivery systems is their targeting ability. This is more prominent in cancer treatment, where the utilizing drugs are highly cytotoxic. Therefore, an effective tumor targeting not only can enhance therapeutic effects of drugs via higher accumulation in tumors, but also can decrease their side effects. In the present work, the designed system is modified with FOA, a popular targeting agent used in cancer therapy [11]. Then, the biodistribution of the RGO-PDA-BSA/**FOA**-DTPA-Mn(II) (FOA-*targeted*) system, in comparison with RGO-PDA-BSA-DTPA-Mn(II) (non-*targeted*) system, is studied in the mice 24 h after intravenous (i.v) injection (Section 2.9). Interesting results were obtained via histopathological examinations (Fig. 3, Panels A to C). The images of reference organs are presented in the panels A (reference or blank organs, obtained from the animals that have been injected with blank PBS). The image of animal organs injected with *non-targeted* system are presented in the Panels B. Some vacuoles, which contain black material, are observed at the inner of the cells. It seems that they are probably filled with the system. The *liver* and *spleen* sections of the mice injected with the *non-targeted*
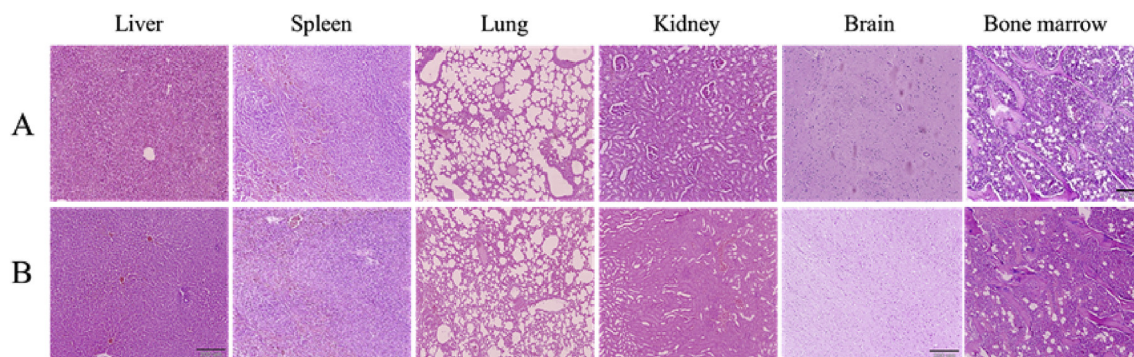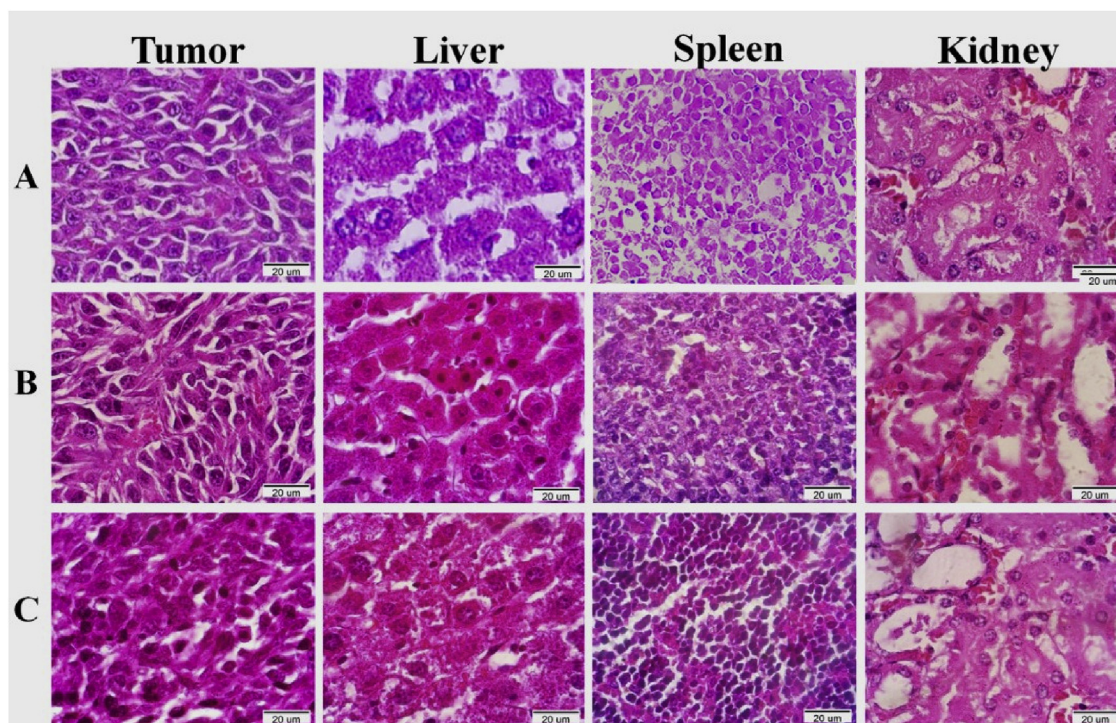

Fig. 2. The microscopic histological photographs recorded for H&E stained sections of vital organs of the mice treated with (A) RGO-PDA-BSA/FOA-DTPA-Mn(II) *system*, and (B) the same volume of PBS used as a control group. No sign of toxicity is apparent. The photographs have been recorded 20 days after intravenous (i.v) injection of 1.5 mg system/kg animal.

Fig. 3. The microscopic histological photographs obtained from H&E stained sections of vital organs of the mice to *assess the role of FOA* in biodistribution of RGO-PDA-BSA/FOA-DTPA-Mn(II) system: The organs of mice injected with (A) PBS without system (reference or blank organs), (B) RGO-PDA-BSA-DTPA-Mn(II) system (having no FOA, non-targeted), and (C) RGO-PDA-BSA/FOA-DTPA-Mn(II) system (having FOA, FOA-targeted). The photographs have been recorded 24 h after i.v injection of 1.5 mg of (A) or (B) systems/kg animal.

system exhibited higher number of black vacuoles (Panels B) in comparison with those injected with the *FOA-targeted* system (Panels C). Instead, the *tumor* sections of the mice injected with *FOA-targeted* system (Panels C) exhibited *more* accumulation of black materials in comparison with those injected with the *non-targeted* system (Panels B).

Therefore, it can be concluded that modification of the RGO-PDA-BSA-DTPA-Mn(II) system with *FOA targeting* agent has caused more efficient delivery of the system into the tumors instead of the vital organs. It means that the FOA-targeted system has exhibited more efficient biodistribution for anti-cancer drug delivery purposes in comparison with non-targeted system. We have to mention that *no black dot containing vacuole* was observed at kidney sections of both injected groups (Fig. 3, groups B and C). These observations support the delivery and therapeutic efficacy of the fabricated system.

3.3.2. Biodistribution assessment based on ICP-OES analysis of the mice organs

The CT-26 colon cancer-bearing mice were sacrificed after 24 h from i.v injection of the system. Then, the important organs of the mice including tumor, liver, kidney, and spleen were extracted and digested in Aqua Regia; then, the acquired solutions were analyzed by ICP-OES for Mn(II) content (Section 2.10). According to the obtained results, the highest Mn(II) ions uptake was observed in the CT-26 tumor (Fig. 4). It means that *the system decorated with FOA*, RGO-PDA-BSA/**FOA**-DTPA-Mn(II) *system is distributed mainly into the tumors, and thus, it is highly efficient for targeted drug delivery into the CT-26 colon tumors.*

3.4. Magnetic resonance imaging

Development of new theranostic systems, as mentioned in the Introduction section, is of significant clinical importance [12]. One way to approach this problem is looking for appropriate designs allowing to attach the therapy, diagnostic and targeting molecules simultaneously onto one single platform, to achieve nano-sized targeted theranostic
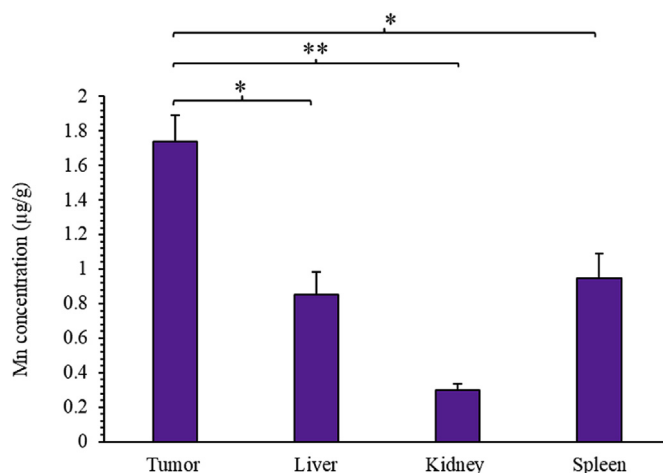
Fig. 4. The quantitative data (μg of Mn(II) found in g of digested organ) obtained via ICP-OES analysis for assessment of the biodistribution of RGO-PDA-BSA/FOA-DTPA-Mn(II) system in CT-26 tumor-bearing mice 24 h after i.v injection of the system (1.5 mg/kg). *:$P < 0.05$, **:$P < 0.005$.

systems [41,42]. The systems containing Mn(II) ions have recently received great attentions as MRI contrast agents, because of lower nephrogenic toxicity, compared with those containing Gd(III) ions [25,43]. The RGO-PDA-BSA/FOA-DTPA-Mn(II) system is expected to have an enhanced MRI contrast effect based on Mn(II) ion characteristics, thus, it is tested for this purpose by *in-vitro* and *in-vivo* methods as follows:

(i) *In-vitro study*: To study the potential use of RGO-PDA-BSA/FOA-DTPA-Mn(II) system as a new MRI CA, the response of system was recorded by using a 1.5 T MRI scanner (Section 2.7). The MRI images became brighter with the increase of Mn(II) concentration in the suspension solution of system (Fig. 5A). A value of $14.7 \, \mathrm{mM^{-1} \, s^{-1}}$ was
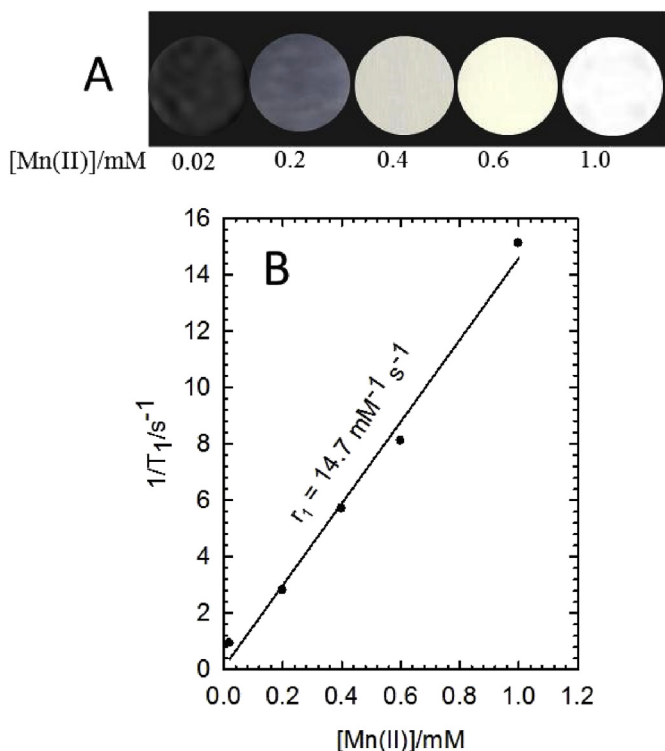
Fig. 5. (A) The MRI T_1-weighted images of RGO-PDA-BSA/FOA-DTPA-Mn(II) system in PBS, pH 7.4, as a function of Mn(II) concentration in the suspension solution of the system, and (B) invers of corresponding T_1 (i.e. relaxation rate) of the system as a function of Mn(II) concentration.

obtained for the relaxivity r_1 ($mM^{-1} s^{-1}$) by the linear approximation of $1/T_1$ vs. Mn(II) concentration (Fig. 5B), supporting the ability of the fabricated drug system for enhancement of the MRI contrast. However, it is difficult to compare the obtained r_1 with those are available for the reported contrast agents, since the related relaxivities have been measured in different field strengths [44]. One should note that the value obtained for r_1 depends on the strength of the employed magnetic field.

(ii) *In-vivo study of non-tumor-bearing male Wistar rats*: Although, the approaches based on *in-vitro* MRI relaxometry measurements are useful for analysis of contrast agents, but they do not fully represent the results of *in-vivo* environment [45]. Accordingly, the *in-vivo* MRI experiments were conducted by non-tumor-bearing male Wistar rats. The MR images were acquired before and after the i.v injection of the system. An obvious T1-weighed contrast, non-selectively developed and enhanced, is observed after 1 h, 3 h and 6 h of injection (Fig. 6, Panels B, C, and D) compared with non-injected rats (Fig. 6, Panel A).

(iii) *In-vivo study of CT-26 tumor-bearing mice*: To evaluate the tumor targeting efficacy of the system, it was utilized to enhance the MRI contrast of CT-26 tumors. As illustrated in Fig. 7, significant contrast effects at the tumor was observed after injection of the targeted system. Therefore, the system has been *selectively delivered* into the tumor and *enhanced the contrast* compared with the surrounding tissues. *These results approve the ability of the* RGO-PDA-BSA/FOA-DTPA-Mn(II) *system as a promising targeted MRI contrast agent for tumor targeting.*

3.5. Assessment of drug delivery and therapeutic efficacy of RGO-PDA-BSA/FOA-DTPA-Mn(II)/5Fu system, in-vitro/in-vivo

Inspired by tumor targeting ability of the RGO-PDA-BSA/FOA-DTPA-Mn(II) system, which is supported by histopathological results (Fig. 2), ICP-OES (Fig. 4), and MR images (Figs. 5 and 6); the drug delivery potential of the system is verified by drug release experiments of the immobilized 5Fu (*a model of anticancer drug*) as RGO-PDA-BSA/FOA-DTPA-Mn(II)/5Fu through (i) *in-vitro* (Fig. 8) and (ii) *in-vivo* (Fig. 9) measurements.

(i) *In-vitro*; The amount of 5Fu loaded by the system was found as 81(± 7) mass% (Section S1(V)). The results show that ~75% of immobilized 5Fu has been released (Section 2.5) from the systems during the first 5 h of incubation time at pH 7.4, with essentially no further release for longer times (Fig. 8).
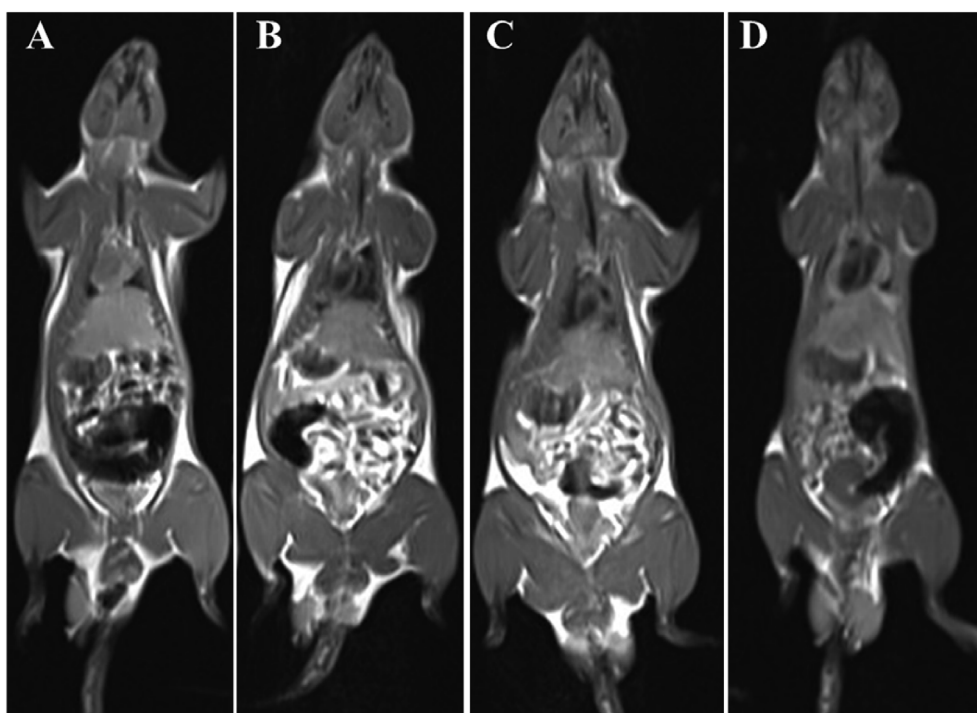

Fig. 6. The T1-weighted MRI images (coronal view) of male Wistar rats; before (A), and after (B) 1 h, (C) 3 h, and (D) 6 h i.v injection of RGO-PDA-BSA/FOA-DTPA-Mn(II) system (1.5 mg/kg).
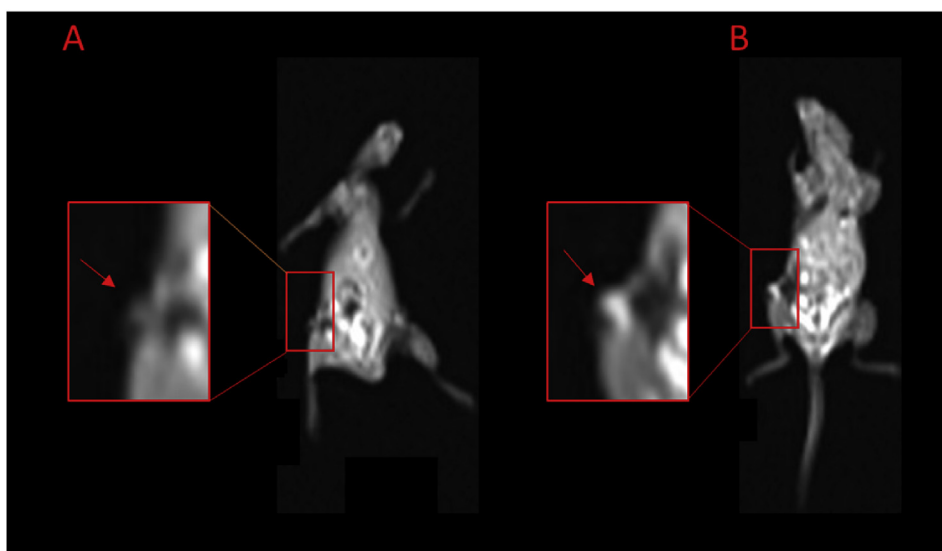
Fig. 7. The T1-weighted MRI images of the BALB/c mice bearing subcutaneous CT-26 tumor at the left flank (A) before and (B) 3 h after i.v injection of RGO-PDA-BSA/FOA-DTPA-Mn(II) system (1.5 mg/kg).
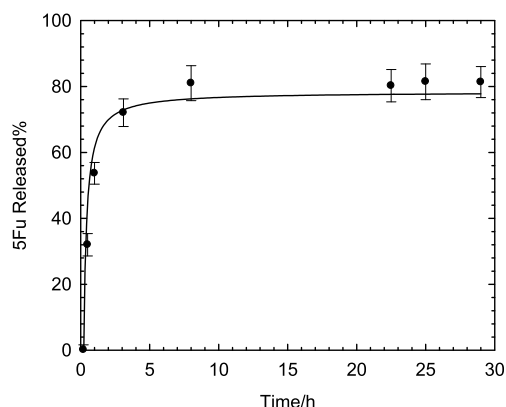

Fig. 8. The 5Fu release results obtained for RGO-PDA-BSA/FOA-DTPA-Mn(II)/5Fu system in 0.05 M PBS at pH 7.4 at different time intervals. Error bars are obtained using at least three measurements.

(ii) *In-vivo*: The CT-26 tumor-bearing mice were treated with different regimes including i.v injection of (a) the PBS, (b) the RGO-PDA-BSA/FOA-DTPA-Mn(II) (1.5 mg/kg) (*without* 5Fu), (c) the *pure* 5Fu (1.2 mg/kg), and (d) the RGO-PDA-BSA/FOA-DTPA-Mn(II)/5Fu (1.5 mg/kg). It should be noted that the amount of injected 5Fu in both cases; RGO-PDA-BSA/FOA-DTPA-Mn(II)/5Fu and 5Fu treated groups, has been the same (Section 2.11). Then, the tumor growth progression was monitored for 3 weeks (Fig. 9). While, the PBS and RGO-PDA-BSA/FOA-DTPA-Mn(II) treatments could not significantly inhibit the development of tumors (curves a and b), the RGO-PDA-BSA/FOA-DTPA-Mn(II)/5Fu inhibited successfully the growth of tumors (curve d), even more effective than the *pure* 5Fu (curve c). *The findings are interesting; supporting ability of the designed drug delivery (theranostic) system for both the enhancement of contrast (diagnosis) and the inhibition of cancer cells growth (therapy).*

4. Conclusion

A MRI contrast agent, DTPA-Mn(II), and a targeting agent, FOA, were integrated onto a drug carrying platform; composed of *biocompatible constituents*, RGO-PDA-BSA. The constructed system, RGO-
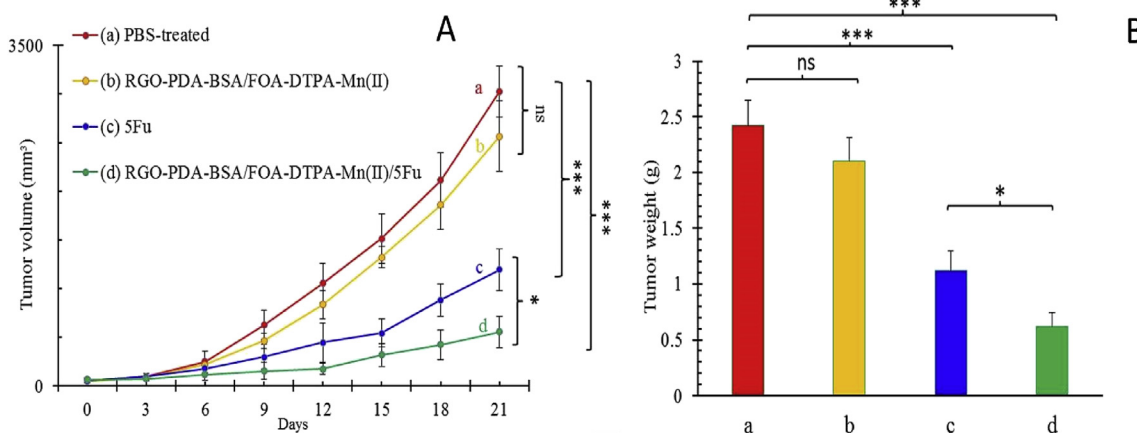

Fig. 9. Drug delivery efficacy of RGO-PDA-BSA/FOA-DTPA-Mn(II)/5Fu system by comparison of the (a) PBS (control test), (b) RGO-PDA-BSA/FOA-DTPA-Mn(II), (c) 5Fu, and (d) RGO-PDA-BSA/FOA-DTPA-Mn(II)/5Fu treatments according to the therapeutic effect on CT-26 colon cancer growth. (**A**) Tumor growth progression obtained for different treatments, and (**B**) mean tumor weight obtained for different treatments at the 21st day of follow up. The ns, one and three asterisk (*) marks on Panel B show not significant, P < 0.05 and P < 0.001, respectively.

PDA-BSA/FOA-DTPA-Mn(II), *enhanced the contrast of cancer cells*, *loaded efficiently* and *transferred selectively* the 5Fu anticancer drug into the CT-26 tumors.

The physicochemical measurements in conjunction with data obtained by electrochemical techniques supported *successful construction* of the RGO-PDA-BSA/FOA-DTPA-Mn(II) system. The *histopathological examinations* demonstrated high *biocompatibility* of the system.

In addition, histopathological examinations and ICP-OES analysis of the injected mice organs approved that the FOA targeted system has significantly more efficient biodistribution for anti-cancer drug delivery purposes compared with non-targeted system.

In-vitro and *in-vivo* MRI and therapy examinations supported the ability of the RGO-PDA-BSA/FOA-DTPA-Mn(II)/5Fu system for both the *enhancement of contrast* (*diagnosis*) and the *inhibition of cancer cells growth* (*therapy*).

Conflicts of interest

We do not have any conflicts of interest to declare.

Acknowledgment

Appendix A. Supplementary data

Supplementary data to this article can be found online at https://doi.org/10.1016/j.jddst.2019.101223.

References

[1] J. Zhang, C.Q. Lan, M. Post, B. Simard, Y. Deslandes, T.H. Hsieh, Design of nanoparticles as drug carriers for cancer therapy, Cancer Genom. Proteom. 3 (2006) 147–157.

[2] S. Krol, R. Macrez, F. Docagne, G. Defer, S. Laurent, M. Rahman, M.J. Hajipour, P.G. Kehoe, M. Mahmoudi, Therapeutic benefits from nanoparticles: the potential significance of nanoscience in diseases with compromise to the blood brain barrier, Chem. Rev. 113 (2012) 1877–1903.

[3] Z.-R. Lu, P. Qiao, Drug delivery in cancer therapy, quo vadis? Mol. Pharm. 15 (2018) 3603–3616.

[4] D. Peer, J.M. Karp, S. Hong, O.C. Farokhzad, R. Margalit, R. Langer, Nanocarriers as an emerging platform for cancer therapy, Nat. Nanotechnol. 2 (2007) 751–760.

[5] W.H. De Jong, P.J. Borm, Drug delivery and nanoparticles: applications and hazards, Int. J. Nanomed. 3 (2008) 133–149.

[6] L. Jabr-Milane, L. van Vlerken, H. Devalapally, D. Shenoy, S. Komareddy, M. Bhavsar, M. Amiji, Multi-functional nanocarriers for targeted delivery of drugs and genes, J. Control. Release 130 (2008) 121–128.

[7] X. Sun, Z. Liu, K. Welsher, J.T. Robinson, A. Goodwin, S. Zaric, H. Dai, Nano-graphene oxide for cellular imaging and drug delivery, Nano Res. 1 (2008) 203–212.

[8] O.C. Farokhzad, R. Langer, Impact of nanotechnology on drug delivery, ACS Nano 3 (2009) 16–20.

[9] A.L. Jackman, C.P. Leamon, Targeted Drug Strategies for Cancer and Inflammation, Springer Science & Business Media, 2011.

[10] Y. Lu, P.S. Low, Folate-mediated delivery of macromolecular anticancer therapeutic agents, Adv. Drug Deliv. Rev. 64 (2012) 342–352.

[11] R. Karimi Shervedani, F. Yaghoobi, M. Torabi, M. Samiei Foroushani, Nanobioconjugated system formed of folic acid–deferrioxamine–Ga (III) on gold surface: preparation, characterization, and activities for capturing of mouse breast cancer cells 4T1, J. Phys. Chem. C 120 (2016) 23212–23220.

[12] R. Karimi Shervedani, F. Yaghoobi, M. Torabi, F.R. Rahsepar, M.S. Foroushani, Controlled synthesis of mixed molecular nanostructures from folate and deferrioxamine-Ga (III) on gold and tuning their performance for cancer cells, Bioelectrochemistry 122 (2018) 149–157.

[13] M. Liong, J. Lu, M. Kovochich, T. Xia, S.G. Ruehm, A.E. Nel, F. Tamanoi, J.I. Zink, Multifunctional inorganic nanoparticles for imaging, targeting, and drug delivery, ACS Nano 2 (2008) 889–896.

[14] A. Fernandez-Fernandez, R. Manchanda, A.J. McGoron, Theranostic applications of nanomaterials in cancer: drug delivery, image-guided therapy, and multifunctional platforms, Appl. Biochem. Biotechnol. 165 (2011) 1628–1651.

[15] J.V. Jokerst, S.S. Gambhir, Molecular imaging with theranostic nanoparticles, Acc. Chem. Res. 44 (2011) 1050–1060.

[16] R. Karimi Shervedani, M.S. Foroushani, A. Kefayat, M. Torabi, F.R. Rahsepar, Construction and characterization of a theranostic system based on graphene/manganese chelate, Biosens. Bioelectron. 117 (2018) 794–801.

[17] M. Zhang, Y. Cao, Y. Chong, Y. Ma, H. Zhang, Z. Deng, C. Hu, Z. Zhang, Graphene oxide based theranostic platform for T_1-weighted magnetic resonance imaging and drug delivery, ACS Appl. Mater. Interfaces 5 (2013) 13325–13332.

[18] H.-W. Yang, C.-Y. Huang, C.-W. Lin, H.-L. Liu, C.-W. Huang, S.-S. Liao, P.-Y. Chen, Y.-J. Lu, K.-C. Wei, C.-C.M. Ma, Gadolinium-functionalized nanographene oxide for combined drug and microRNA delivery and magnetic resonance imaging, Biomaterials 35 (2014) 6534–6542.

[19] M. Orecchioni, R. Cabizza, A. Bianco, L.G. Delogu, Graphene as cancer theranostic tool: progress and future challenges, Theranostics 5 (2015) 710–723.

[20] Y. Liu, K. Ai, L. Lu, Polydopamine and its derivative materials: synthesis and promising applications in energy, environmental, and biomedical fields, Chem. Rev. 114 (2014) 5057–5115.

[21] C. Cheng, S. Nie, S. Li, H. Peng, H. Yang, L. Ma, S. Sun, C. Zhao, Biopolymer functionalized reduced graphene oxide with enhanced biocompatibility via mussel inspired coatings/anchors, J. Mater. Chem. B 1 (2013) 265–275.

[22] F. Kratz, Albumin as a drug carrier: design of prodrugs, drug conjugates and nanoparticles, J. Control. Release 132 (2008) 171–183.

[23] E. Frei, Albumin binding ligands and albumin conjugate uptake by cancer cells, Diabetol. Metab. Syndrome 3 (2011) 1–4.

[24] D. Wang, N. Gan, H. Zhang, T. Li, L. Qiao, Y. Cao, X. Su, S. Jiang, Simultaneous electrochemical immunoassay using graphene–Au grafted recombinant apoferritin-encoded metallic labels as signal tags and dual-template magnetic molecular imprinted polymer as capture probes, Biosens. Bioelectron. 65 (2015) 78–82.

[25] D. Pan, A.H. Schmieder, S.A. Wickline, G.M. Lanza, Manganese-based MRI contrast agents: past, present and future, Tetrahedron 67 (2011) 8431.

[26] Y. Wu, Z. Deng, H. Wang, W. Ma, C. Zhou, S. Zhang, Repeated cycles of 5-fluorouracil chemotherapy impaired anti-tumor functions of cytotoxic T cells in a CT26 tumor-bearing mouse model, BMC Immunol. 17 (2016) 29.

[27] R. Karimi Shervedani, E. Ansarifar, M.S. Foroushani, Electrocatalytic activities of graphene/nile blue nanocomposite toward determination of hydrogen peroxide and nitrite ion, Electroanalysis 28 (2016) 1957–1969.

[28] M.M. Tomayko, C.P. Reynolds, Determination of subcutaneous tumor size in athymic (nude) mice, Cancer Chemother. Pharmacol. 24 (1989) 148–154.

[29] B. Yang, Z. Liu, Z. Guo, W. Zhang, M. Wan, X. Qin, H. Zhong, In situ green synthesis of silver–graphene oxide nanocomposites by using tryptophan as a reducing and stabilizing agent and their application in SERS, Appl. Surf. Sci. 316 (2014) 22–27.

[30] L.Q. Xu, W.J. Yang, K.-G. Neoh, E.-T. Kang, G.D. Fu, Dopamine-induced reduction and functionalization of graphene oxide nanosheets, Macromolecules 43 (2010) 8336–8339.

[31] I. Cha, E.J. Lee, H.S. Park, J.-H. Kim, Y.H. Kim, C. Song, Facile electrochemical synthesis of polydopamine-incorporated graphene oxide/PEDOT hybrid thin films for pseudocapacitive behaviors, Synth. Met. 195 (2014) 162–166.

[32] G. Ciofani, V. Raffa, A. Menciassi, A. Cuschieri, Folate functionalized boron nitride nanotubes and their selective uptake by glioblastoma multiforme cells: implications for their use as boron carriers in clinical boron neutron capture therapy, Nanoscale Res. Lett. 4 (2009) 113–121.

[33] X. Fan, G. Jiao, W. Zhao, P. Jin, X. Li, Magnetic Fe_3O_4–graphene composites as targeted drug nanocarriers for pH-activated release, Nanoscale 5 (2013) 1143–1152.

[34] M. Gaumet, A. Vargas, R. Gurny, F. Delie, Nanoparticles for drug delivery: the need for precision in reporting particle size parameters, Eur. J. Pharm. Biopharm. 69 (2008) 1–9.

[35] V. Bliznyuk, N. Conroy, Y. Xie, R. Podila, A. Rao, B.A. Powell, Increase in the reduction potential of uranyl upon interaction with graphene oxide surfaces, Phys. Chem. Chem. Phys. 20 (2018) 1752–1760.

[36] J.-l. Wang, B.-c. Li, Z.-j. Li, K.-f. Ren, L.-j. Jin, S.-m. Zhang, H. Chang, Y.-x. Sun, J. Ji, Electropolymerization of dopamine for surface modification of complex-shaped cardiovascular stents, Biomaterials 35 (2014) 7679–7689.

[37] A. Pontinha, S. Jorge, V. Diculescu, M. Vivan, A. Oliveira-Brett, Antineoplasic drug methotrexate redox mechanism using a glassy carbon electrode, Electroanalysis 24 (2012) 917–923.

[38] G.S. Loving, S. Mukherjee, P. Caravan, Redox-activated manganese-based MR contrast agent, J. Am. Chem. Soc. 135 (2013) 4620–4623.

[39] X. Hua, X. Hou, X. Gong, G. Shen, Electrochemical behavior of 5-fluorouracil on a glassy carbon electrode modified with bromothymol blue and multi-walled carbon nanotubes, Anal. Methods 5 (2013) 2470–2476.

[40] K. Yang, S. Zhang, G. Zhang, X. Sun, S.-T. Lee, Z. Liu, Graphene in mice: ultrahigh in vivo tumor uptake and efficient photothermal therapy, Nano Lett. 10 (2010) 3318–3323.

[41] M. Malakoutikhah, M. Teixidó, E. Giralt, Shuttle-mediated drug delivery to the brain, Angew. Chem. Int. Ed. 50 (2011) 7998–8014.

[42] E. Boisselier, D. Astruc, Gold nanoparticles in nanomedicine: preparations, imaging, diagnostics, therapies and toxicity, Chem. Soc. Rev. 38 (2009) 1759–1782.

[43] M. Kueny-Stotz, A. Garofalo, D. Felder-Flesch, Manganese-enhanced MRI contrast agents: from small chelates to nanosized hybrids, Eur. J. Inorg. Chem. (2012) 1987–2005 2012.

[44] T. Kim, E. Momin, J. Choi, K. Yuan, H. Zaidi, J. Kim, M. Park, N. Lee, M.T. McMahon, A. Quinones-Hinojosa, Mesoporous silica-coated hollow manganese oxide nanoparticles as positive T_1 contrast agents for labeling and MRI tracking of adipose-derived mesenchymal stem cells, J. Am. Chem. Soc. 133 (2011) 2955–2961.

[45] D. Högemann, V. Ntziachristos, L. Josephson, R. Weissleder, High throughput magnetic resonance imaging for evaluating targeted nanoparticle probes, Bioconjug. Chem. 13 (2002) 116–121.